Novel Gaussian Mixture Model based Nonsingular Terminal Sliding Mode Control for Spacecraft Close-range Proximity with Complex Shape Obstacle

Yi Wang[1, 4], Wen Yao[1], Xiaoqian Chen[1], Matteo Ceriotti[2], Yuzhu Bai[3] & Xiaozhou Zhu[1,*]

[1] National Innovation Institute of Defense Technology, Chinese Academy of Military Sciences, Beijing, 100071, China;

[2] School of Engineering, University of Glasgow, Glasgow G12 8QQ, United Kingdom;

[3] College of Aerospace and Engineering, National University of Defense Technology, Changsha 410073, China;

[4] Nanjing Institute of Electronic Technology, Nanjing 210039, China.

Corresponding author: Xiaozhou Zhu, zhuxiaozhou10@nudt.edu.cn.

Abstract： This paper is mainly focusing on the problem of spacecraft close-range proximity with obstacle avoidance in the presence of complex shape. A novel Gaussian Mixture Model based nonsingular terminal sliding mode control (GMM-NTSMC) is proposed. This is achieved by developing GMM-based potential function with a switching surface of NTSMC. It is theoretically proved that the closed-loop system is global stable. The main contribution of this paper is that the GMM-based avoiding strategies, which include the GMM-based terminal sliding mode control (GMM-TSMC) and GMM-NTSMC, can solve the collision avoidance problem considering complex shape while the artificial potential function based terminal sliding model control (APF-TSMC) fails. Moreover, the GMM-NTSMC and the GMM-TSMC require less energy with respect to the APF-TSMC. Furthermore, the GMM-NTSMC retains the advantage of the NTSMC and can avoid singularity problem while GMM-TSMC cannot. Finally, numerical simulations are performed to verify the effectiveness and superiority of the proposed GMM-NTSMC.

Keywords：Spacecraft close-range proximity, Gaussian Mixture Model, obstacle avoidance, complex shape, artificial potential function.

1 Introduction

In recent years, on-orbit failures have exceeded launch failures, the most common failures of space missions in the past, and cumulatively account for losses of billions of dollars [1, 2]. Among them, many fails are caused by parts and materials failure. Furthermore, most of these failure occur in telemetry, tracking and command (TTC) subsystems [1]. For example, without any assistance from ground personnel, Demonstration of Autonomous Rendezvous Technology (DART) [3] rendezvoused with and performed a variety of maneuvers in close-proximity to the Multi-Paths-Beyond-Line-of-Sight- Communications (MUBLCOM). However, the GPS receiver of DART suffered from a factory error and caused DART to resent its position and velocity continually. Hence, low-velocity collision between DART and MUBLCOM happens. In addition, one of Intelsat New Dawn's antennas failed to deploy, and hence prevented the utilization of the C-band payload and limited the operational lifespan of the spacecraft. Thus, the spacecraft close-range proximity and the space maintenance should be executed. For these examples, the space maintenance of TTC subsystem is in high demand in space missions that enhances the operational lifetime and capability of space assets [4, 5]. Moreover, spacecraft close-range proximity maneuver is a key technology for space asset maintenance, and hence it has attracted a lot of research.

During the spacecraft close-range proximity maneuvers, the stringent safety is among the most critical requirements, and hence it is notable that such complex space missions have motivated the development of collision avoidance technologies. Many researchers [6-10] transformed the collision avoidance problem into a constrained optimization problem, and applied optimization algorithms [6-10]

to design safe trajectories. However, because of the high computational burden, applications of these methods are limited. To decrease the computational burden, the artificial potential field (APF) method [11-16] has been widely utilized for obstacle avoidance, which utilizes the negative gradient of the potential function to generate the simple analytical control law. Nevertheless, the collision could still happen in the spacecraft close-range proximity scenarios confronted with complex shapes [17-19]. In particular, due to the existence of sizeable protruding (e.g. an antenna), the complexity of spacecraft's shape increases and the difficulty of the collision avoidance problem is enlarged. In terms of collision avoidance problem with APF method, although some researchers [18-20] solve them in the presence of the simple geometries, the collision avoidance problem in the presence of complex shape is urgent to be solved.

To solve the abovementioned problem, a novel GMM-NTSMC is proposed for spacecraft close-range proximity in the presence of complex shape. GMM has attracted much attention in some areas, such as model construction [21, 22], uncertainty propagation [23, 24], fault detection [25] and so on. The core idea of GMM is to approximate arbitrary probability density functions with finite sum of weighted Gaussian density functions. In addition, as the nonsingular terminal sliding mode control (NTSMC) [26] has strong robustness performance and has some advantages, such as easy implementation, no singularity problem, and making the system states reach the control objective point in finite time, this NTSMC has been widely applied. In this paper, based the *K*-means [27] and Expectation Maximization (EM) [28] algorithm, the GMM-based potential function is developed. Besides, as the NFTSMC [26] requires much fuel cost and the fuel cost is an important criterion to assess the superiority of the proposed control laws in space mission, the NTSMC is utilized in this paper. Then, combined the developed potential function with the TSMC and NTSMC, the GMM-TSMC and GMM-NTSMC are designed. Moreover, a Lyapunov-based analysis verifies the stability of the overall closed-loop system. Compared with the traditional APF, the available parameters of the complex shape obtained by the GMM method

are included in the GMM-based potential function. Thus, the GMM-based avoidance strategies can solve the collision avoidance problem considering complex shape. Moreover, the GMM-NTSMC and the GMM-TSMC require less energy with respect to the APF-TSMC [12, 29]. Though the GMM-NTSMC requires more energy than the GMM-TSMC, the GMM-NTSMC retains the advantage of the NTSMC and can avoid singularity problem while GMM-TSMC cannot.

The structure of this paper is as follows. The dynamics of spacecraft relative motion is introduced and the novel GMM-based potential function is defined in Section 2. In Section 3, the GMM-NTSMC is designed to generate the control law. Next, the simulation results and its discussion are shown in Section 4. The study's conclusions are presented in Section 5.

2 Gaussian-Mixture-Model-based Potential Function

This section illustrates the spacecraft relative motion dynamics. The O_I-$X_IY_IZ_I$ frame is an inertial frame located in the center of the Earth. The local-vertical-local-horizontal (LVLH) coordinate frame [30, 31] is used to depict the spacecraft relative motion. Furthermore, a state transition matrix [32, 33] for the nonlinear problem of relative motion on an arbitrary elliptical orbit is described as

$$\ddot{\boldsymbol{r}} = \boldsymbol{A}\boldsymbol{r} + \boldsymbol{B}\dot{\boldsymbol{r}} + \boldsymbol{u}, \tag{1}$$

where $\boldsymbol{r} = [x, y, z]^{\mathrm{T}}$ and $\dot{\boldsymbol{r}} = [\dot{x}, \dot{y}, \dot{z}]^{\mathrm{T}}$ represent the deputy spacecraft's relative position and the relative velocity with respect to the chief spacecraft in the LVLH coordinate, respectively. $\boldsymbol{u} = [u_x, u_y, u_z]^{\mathrm{T}}$ is the control acceleration. The matrix $\boldsymbol{A}$ and $\boldsymbol{B}$ are given as [32, 33]

$$\boldsymbol{A} = \begin{bmatrix} \dot{\omega}^2 + 2\dfrac{\mu}{r_c^3} & \dot{\omega} & 0 \\ -\dot{\omega} & \omega^2 - \dfrac{\mu}{r_c^3} & 0 \\ 0 & 0 & -\dfrac{\mu}{r_c^3} \end{bmatrix}, \tag{2}$$

$$\boldsymbol{B}=\begin{bmatrix} 0 & 2\omega & 0 \\ -2\omega & 0 & 0 \\ 0 & 0 & 0 \end{bmatrix}, \tag{3}$$

where μ is gravitational constant of the Earth and r_c is the relative distance between the Earth and the chief spacecraft. *f* represents the true anomaly of the chief spacecraft. *a* is the semi-major axis and *e* is the eccentricity of the chief spacecraft. ω, $\dot{\omega}$ represent the angular velocity and angular acceleration of the chief spacecraft, which is computed as [32, 33]

$$\omega=\frac{\left(1+e\cos f\right)^2}{\left(1-e^2\right)^{\frac{3}{2}}}\sqrt{\frac{\mu}{a^3}}, \tag{4}$$

$$\dot{\omega}=\frac{2\mu\left(1+e\cos f\right)^3 e\sin f}{a^3\left(1-e^2\right)^{\frac{3}{2}}}. \tag{5}$$

As the GMM method is the parametric form that conveys higher level statistical geometric entities, the GMM is achieved based on the simulated feature points in the surface of the target object. Thus, the parametric form provides a tractable statistical representation for 3D reconstruction. Given that a set of *N* point samples $\boldsymbol{Z}=\left\{\boldsymbol{Z}_i=\left[x_i,y_i,\boldsymbol{z}_i\right]^{\mathrm{T}}\right\}$ of the complex shape chief spacecraft's surface, the cluster parameter Θ of an unknown world model is searched to describe $\boldsymbol{Z}$. In this paper, a combination of *K* Gaussian probability distribution functions or mixtures is chosen to parameterize Θ. Then, using the Gaussian Mixture Model [21, 22], the probability of each individual point in the point cloud $\boldsymbol{Z}_i$ is defined as

$$p\left(\boldsymbol{Z}_i\mid\Theta\right)=\sum_{j=1}^{K}\pi_j\mathcal{N}\left(\boldsymbol{Z}_i\mid\boldsymbol{\mu}_j,\boldsymbol{\Sigma}_j\right) \tag{6}$$

where π_j represents the mixing weights, and $\sum_{j=1}^{K}\pi_j=1$, K is the number of Gaussian distribution functions. Each Gaussian has nine free parameters representing its mean value $\boldsymbol{\mu}_j$ (three) and covariance matrix $\boldsymbol{\Sigma}_j$ (six, due to symmetry). $\Theta=\left\{\Theta_j=\left(\pi_j,\mu_j,\boldsymbol{\Sigma}_j\right)\right\}\left(j=1,2,\ldots,K\right)$ is the parameter sets of the Gaussian Mixture Model. $\boldsymbol{r}_1$ represents the relative position vector of the point samples. $\mathcal{N}(\bullet)$ is the multivariate (3D) Gaussian probability distribution, which is [21, 22]

$$\mathcal{N}\left(\boldsymbol{Z}_i\mid\boldsymbol{\mu}_j,\boldsymbol{\Sigma}_j\right)=\frac{1}{2\pi\left|\boldsymbol{\Sigma}_j\right|^{1/2}}e^{-\frac{1}{2}\left(\boldsymbol{Z}_i-\boldsymbol{\mu}_j\right)^{\mathrm{T}}\boldsymbol{\Sigma}_j^{-1}\left(\boldsymbol{Z}_i-\boldsymbol{\mu}_j\right)} \tag{7}$$

Subsequently, the *K*-means clustering algorithm [21, 27] is applied to determine the raw centers of clustering data and the Expectation-Maximization (EM) algorithm [28] is utilized to iteratively estimate the cluster parameters Θ in Eq.(6). With the estimated Θ, the Gaussian Mixture Model is obtained. Furthermore, the deputy spacecraft is assumed to be a massless particle. Similarly to the Gaussian Mixture Model, a novel GMM-based potential function that takes into account a complex shape is proposed here and is given as

$$V_0\left(\boldsymbol{r},\Theta\right)=\sum_{j=1}^{K}\frac{\pi_j}{2\pi\left|\boldsymbol{\Sigma}_j\right|^{1/2}}e^{-\frac{1}{2}\left(\boldsymbol{r}-\boldsymbol{\mu}_j\right)^{\mathrm{T}}\boldsymbol{\Sigma}_j^{-1}\left(\boldsymbol{r}-\boldsymbol{\mu}_j\right)} \tag{8}$$

When the deputy spacecraft arrives at the desired position vector $\boldsymbol{r}_f=\left(x_f,y_f,z_f\right)^{\mathrm{T}}$, the value of the GMM-based function in Eq.(8) is not close to zero and it will lead to the deviation of the desired position and low control accuracy. Thus, to ensure that the value of the GMM-based function is zero, the GMM-based potential function is revised into

$$\varphi=\varphi_a+\varphi_r=\frac{1}{2}\left(\boldsymbol{r}-\boldsymbol{r}_f\right)^{\mathrm{T}}\boldsymbol{P}\left(\boldsymbol{r}-\boldsymbol{r}_f\right)+\frac{1}{2}\left(\boldsymbol{r}-\boldsymbol{r}_f\right)^{\mathrm{T}}\boldsymbol{M}\left(\boldsymbol{r}-\boldsymbol{r}_f\right)\bullet\sum_{j=1}^{K}\frac{\pi_j}{2\pi\left|\boldsymbol{\Sigma}_j\right|^{1/2}}e^{-\frac{1}{2}\left(\boldsymbol{r}-\boldsymbol{\mu}_j\right)^{\mathrm{T}}\boldsymbol{\Sigma}_j^{-1}\left(\boldsymbol{r}-\boldsymbol{\mu}_j\right)} \tag{9}$$

where $\boldsymbol{M}$ and $\boldsymbol{P}$ are positive definite gain matrixes.

3 Gaussian Mixture Model based nonsingular terminal sliding mode control

To obtain a more efficient controller, the NTSMC is combined with GMM-based potential functions. As the NTSMC offers a wide variety of design alternatives for the GMM with low energy cost, a novel GMM-NSTMC scheme is proposed in details and the proof of stability is completed as the followings.

3.1 Design of the switching surface

Using the gradient of GMM-based potential function and the NTSMC [26], the switching surface is designed as

$$\boldsymbol{S} = \boldsymbol{k}_s \nabla_{\boldsymbol{r}} \varphi + \xi_0 \boldsymbol{e} + \xi_1 \boldsymbol{e}^{\tau} + \xi_2 \dot{\boldsymbol{e}}^{p/q} \tag{10}$$

where $\boldsymbol{S}=\begin{bmatrix} S_1 & S_2 & S_3 \end{bmatrix}^{\mathrm{T}}$ is the switching surface, $\boldsymbol{k}_s$ is the positive definite gain matrix. ∇ represents the gradient. $\nabla_{\boldsymbol{r}} \varphi$ is the gradient of the GMM-based potential function φ with respect to the position vector of the deputy spacecraft, and detailed mathematical expressions are shown in **Appendix A1**. $\dot{\boldsymbol{r}}_f \in \Re^{3\times 1}$ is the derivative of $\boldsymbol{r}_f$. The error vector $\boldsymbol{e}=\boldsymbol{r}-\boldsymbol{r}_f$ and $\dot{\boldsymbol{e}}=\dot{\boldsymbol{r}}-\dot{\boldsymbol{r}}_f$ are defined. $\boldsymbol{\xi}_1=\mathrm{diag}\left(\begin{bmatrix} \xi_{11} & \xi_{12} & \xi_{13} \end{bmatrix}\right) \in \Re^{3\times 3}$ and $\boldsymbol{\xi}_2=\mathrm{diag}\left(\begin{bmatrix} \xi_{21} & \xi_{22} & \xi_{23} \end{bmatrix}\right) \in \Re^{3\times 3}$ are positive definite gain matrices, respectively. $\xi_0 < 1$ is a positive gain parameter. p and q are positive odd parameters satisfying the relation $0<p/q<1$ and $\tau > 1$.

Based on Eq.(10), the derivation of the switching surface $\boldsymbol{S}$ is given as

$$\begin{aligned} \dot{\boldsymbol{S}} &= \boldsymbol{k}_s \left(\frac{\partial \nabla_{\boldsymbol{r}} \varphi}{\partial \boldsymbol{r}} \right) \frac{d\boldsymbol{r}}{dt} + \boldsymbol{k}_s \left(\frac{\partial \nabla_{\boldsymbol{r}} \varphi}{\partial \boldsymbol{r}_f} \right) \frac{d\boldsymbol{r}_f}{dt} + \xi_0 \dot{\boldsymbol{e}} + \tau \boldsymbol{\xi}_1 \left| \boldsymbol{e} \right|^{\tau-1} \cdot \dot{\boldsymbol{e}} + \frac{p}{q} \boldsymbol{\xi}_2 \left| \dot{\boldsymbol{e}} \right|^{p/q-1} \cdot \ddot{\boldsymbol{e}} \\ &= \boldsymbol{k}_s \left(\nabla_{\boldsymbol{rr}} \varphi \dot{\boldsymbol{r}} + \nabla_{\boldsymbol{rr}_f} \varphi \dot{\boldsymbol{r}}_f \right) + \xi_0 \dot{\boldsymbol{e}} + \tau \boldsymbol{\xi}_1 \left| \boldsymbol{e} \right|^{\tau-1} \cdot \dot{\boldsymbol{e}} + \frac{p}{q} \boldsymbol{\xi}_2 \left| \dot{\boldsymbol{e}} \right|^{p/q-1} \cdot \ddot{\boldsymbol{e}} \end{aligned} \tag{11}$$

where the mathematical expressions of $\nabla_{\boldsymbol{rr}}\varphi$ and $\nabla_{\boldsymbol{rr}_f}\varphi$ are derived in the **Appendix. A1**.

3.2 Design and analysis of GMM-NTSMC

In this paper, the asymptotic law of the switching surface is chosen as [12, 29]

$$\dot{\boldsymbol{S}} = -\boldsymbol{\lambda}_1\boldsymbol{S} - \boldsymbol{\lambda}_2 sig(\boldsymbol{S})^{\alpha} \tag{12}$$

where $0<\alpha<1$, $\boldsymbol{\lambda}_1$=diag$\left(\left[\lambda_{11} \quad \lambda_{12} \quad \lambda_{13}\right]\right)\in\Re^{3\times3}$ and $\boldsymbol{\lambda}_2$=diag$\left(\left[\lambda_{21} \quad \lambda_{22} \quad \lambda_{23}\right]\right)\in\Re^{3\times3}$ are the positive-definite matrices, the function $sig(\boldsymbol{S})^{\alpha}$ is defined as

$$sig(\boldsymbol{S})^{\alpha} = \left(|S_1|^{\alpha}\,\mathrm{sgn}(S_1) \quad |S_2|^{\alpha}\,\mathrm{sgn}(S_2) \quad |S_3|^{\alpha}\,\mathrm{sgn}(S_3)\right)^{\mathrm{T}} \tag{13}$$

According to Eq.(1), Eq.(11) and Eq.(12), the control law of the GMM-NTSMC is given as

$$\boldsymbol{u} = \frac{q}{p}\frac{1}{\boldsymbol{\xi}_2}|\dot{\boldsymbol{e}}|^{1-p/q}\cdot\left[-\boldsymbol{k}_s\left(\nabla_{\boldsymbol{rr}}\varphi\dot{\boldsymbol{r}} + \nabla_{\boldsymbol{rr}_f}\varphi\dot{\boldsymbol{r}}_f\right) - \boldsymbol{\lambda}_1\boldsymbol{S} - \boldsymbol{\lambda}_2 sig(\boldsymbol{S})^{\alpha} - \xi_0\dot{\boldsymbol{e}} - \tau\boldsymbol{\xi}_1|\boldsymbol{e}|^{\tau-1}\cdot\dot{\boldsymbol{e}}\right] - \boldsymbol{A}\boldsymbol{r} - \boldsymbol{B}\dot{\boldsymbol{r}} + \ddot{\boldsymbol{r}}_f \tag{14}$$

where $\dot{\boldsymbol{r}}_f = [\dot{x}_f, \dot{y}_f, \dot{z}_f]^{\mathrm{T}}$ is the relative velocity of the terminal point,

$$|\dot{\boldsymbol{e}}|^{1-p/q} = \left(\left(\dot{x}-\dot{x}_f\right)^{1-p/q}, \left(\dot{y}-\dot{y}_f\right)^{1-p/q}, \left(\dot{z}-\dot{z}_f\right)^{1-p/q}\right)^{\mathrm{T}} \tag{15}$$

$$|\boldsymbol{e}|^{\tau-1} = \left(\left(x-x_f\right)^{\tau-1}, \left(y-y_f\right)^{\tau-1}, \left(z-z_f\right)^{\tau-1}\right)^{\mathrm{T}} \tag{16}$$

From Eq.(14), the control force of GMM-NTSMC does not contain any negative fractional power since $0<p/q<1$ and $\tau>1$, and thus it is concluded that from any initial origin states, the closed-loop control system has no singularity.

To analyze the stability of the GMM-NTSMC, a Lyapunov function is defined as

$$V_1 = \frac{1}{2}\boldsymbol{S}^{\mathrm{T}}\boldsymbol{S} \geq \boldsymbol{0} \tag{17}$$

Based on Eq.(17),

$$\dot{V}_1 = \boldsymbol{S}^{\mathrm{T}}\dot{\boldsymbol{S}} = -\boldsymbol{S}^{\mathrm{T}}\left(\boldsymbol{\lambda}_1\boldsymbol{S}+\boldsymbol{\lambda}_2 sig\left(\boldsymbol{S}\right)^{\alpha}\right) \le -\lambda_{1\min}\boldsymbol{S}^{\mathrm{T}}\boldsymbol{S} - \lambda_{2\min}\left\|\boldsymbol{S}\right\|^{\alpha+1} \tag{18}$$

where $\lambda_{1\min} = \min\left(\lambda_{1i}\right)\left(i=1,2,3\right)$ and $\lambda_{2\min} = \min\left(\lambda_{2i}\right)\left(i=1,2,3\right)$.

Subsequently, it is concluded that

$$\begin{aligned}\dot{V}_1 &\le -\lambda_{1\min}\boldsymbol{S}^{\mathrm{T}}\boldsymbol{S} - \lambda_{2\min}\left\|\boldsymbol{S}\right\|^{\alpha+1} \le -2\lambda_{1\min}V_1 - \lambda_{2\min}\left(2V_1\right)^{\frac{\alpha+1}{2}} \\ &\le -2\lambda_{1\min}V_1 - \sqrt{2}\lambda_{2\min}V_1^{\frac{1}{2}}\end{aligned} \tag{19}$$

Therefore, by the Lyapunov stability theorem, the system with GMM-NTSMC is stable in finite time [12, 29] and it ensures that the system with any random initial states can reach to the surface $\boldsymbol{S}(t)$ in the finite time T_s. Moreover, based on Eq.(10), the control error $\boldsymbol{e}$ and $\dot{\boldsymbol{e}}$ will converge to zero within the finite time in the terminal switching surface, and then to solve the differential Eq.(10).

In addition, the APF-TSMC (**Appendix A2**) and the GMM-TSMC (**Appendix A3**) is also designed for comparison to show the superiority of the GMM-NTSMC.

4 Numerical simulation

4.1 Simulation Description

To verify the effectiveness of the proposed method for spacecraft close-range proximity with obstacle avoidance in presence of complex shape, the numerical simulations are conducted with APF-TSMC and the designed GMM-TSMC and the proposed GMM-NTSMC. Fig.1 depicts the geometry of the chief and relative motion of the deputy in LVLH frame. In this numerical simulation, the deputy spacecraft need to arrive at the desire point near the antenna of the chief spacecraft. The movement of the deputy begins at asterisk 1, and then flying around asterisk 2, finally arrives at the target asterisk 3. Moreover, the physical parameters of the chief spacecraft and the deputy spacecraft and the initial rela-

tive position and relative velocity of the deputy spacecraft in LVLH frame are given in Table 1 and Table 2, respectively.

Table 1 Physical parameters of the chief spacecraft and the deputy spacecraft

Chief Spacecraft		Deputy Spacecraft	
Parameter	Value	Parameter	Value
Slide length (m)	10	Mass (kg)	50
Solar panel (m) ×2	10 (Long) × 5 (Wide)	Max propulsion (N)	30
Antenna (m) ×2	5		

Table 2 Initial relative position and relative velocity of the deputy spacecraft in LVLH frame

x (m)	y (m)	z (m)	v_x (m/s)	v_y (m/s)	v_z (m/s)
1	-16	0	0	0	0

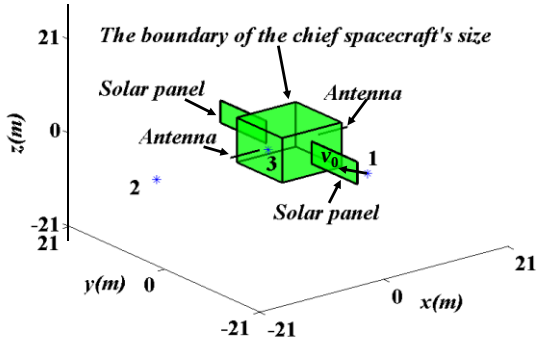

Fig. 1 Geometry of the chief and relative motion of the deputy in LVLH frame.

Furthermore, the desired states $\boldsymbol{X_f}$ for the simulation system are determined as

$$\boldsymbol{X}_f = \begin{bmatrix} -5 & -0.913043 & -0.304348 & 0 & 0 & 0 \end{bmatrix}^{\mathrm{T}} \tag{20}$$

Both the period of the control maneuvers and the integration step are 1 s, and the final time is

$$\boldsymbol{t}_f = 800\,s \tag{21}$$

The semi-major axis and the eccentricity of the orbit of chief spacecraft are 6778.1336 km and 0.01, respectively. The gravitational constant of Earth is $3.986\times 10^{14}\ \mathrm{m^3/s^2}$. The GMM is assumed to consist of 10 components. The initial value for *K*-means is given as

$$\boldsymbol{\mu}_{k0} = \begin{bmatrix} 5 & -5 & 0 & 0 & 0 & 0 & -7.5 & 7.5 & 0 & 0 \\ 0 & 0 & 5 & -5 & 0 & 0 & 0 & 0 & 10 & -10 \\ 0 & 0 & 0 & 0 & 5 & -5 & 0 & 0 & 0 & 0 \end{bmatrix} \tag{22}$$

The control gain and parameters used in all simulation are shown in Eq.(23). It is noted that all the common parameters for the APF-TSMC, GMM-TSMC and GMM-NTSMC are set to be the same.

$$\begin{cases} \psi_i = 1\times 10^{-1},\ \boldsymbol{N}_i = diag\left(\begin{bmatrix} 5.5\times 10^{-4} & 5.5\times 10^{-4} & 5.5\times 10^{-4} \end{bmatrix}\right),\ \sigma_i = 1,\ \alpha = 0.9999 \\ \boldsymbol{\lambda}_1 = diag\left(\begin{bmatrix} 1.5\times 10^{-2} & 1.5\times 10^{-2} & 1.5\times 10^{-2} \end{bmatrix}\right), \\ \boldsymbol{\lambda}_2 = diag\left(\begin{bmatrix} 1\times 10^{-2} & 1\times 10^{-2} & 1\times 10^{-2} \end{bmatrix}\right), \\ \boldsymbol{k}_s = diag\left(\begin{bmatrix} 10 & 6 & 8 \end{bmatrix}\right),\ \boldsymbol{M} = diag\left(\begin{bmatrix} 0.8 & 0.6 & 0.4 \end{bmatrix}\right), \\ \boldsymbol{P} = diag\left(\begin{bmatrix} 1.2\times 10^{-2} & 1.2\times 10^{-2} & 1.2\times 10^{-2} \end{bmatrix}\right) \\ \xi_0 = 0.01,\ \tau = 1.5,\ p = 5,\ q = 7,\ \boldsymbol{\xi}_1 = diag\left(\begin{bmatrix} 1\times 10^{-2} & 1\times 10^{-3} & 1\times 10^{-3} \end{bmatrix}\right) \\ \boldsymbol{\xi}_2 = diag\left(\begin{bmatrix} 1 & 0.8 & 0.8 \end{bmatrix}\right) \end{cases} \tag{23}$$

4.2 Simulation results and analysis

Using the *K*-means with the initial mean in Eq.(22) and EM method, the parameters of the GMM are obtained (**Appendix A4**) and the 3D reconstruction of the chief spacecraft with GMM method is shown in Fig.2. Furthermore, Fig.2a and Fig.2b represent the 3D reconstruction of the chief spacecraft from different angles. Comparing Fig.1 and Fig.2, it is noted that the GMM can provide the tractable statistical representation for 3D reconstruction of the complex shape of the chief.

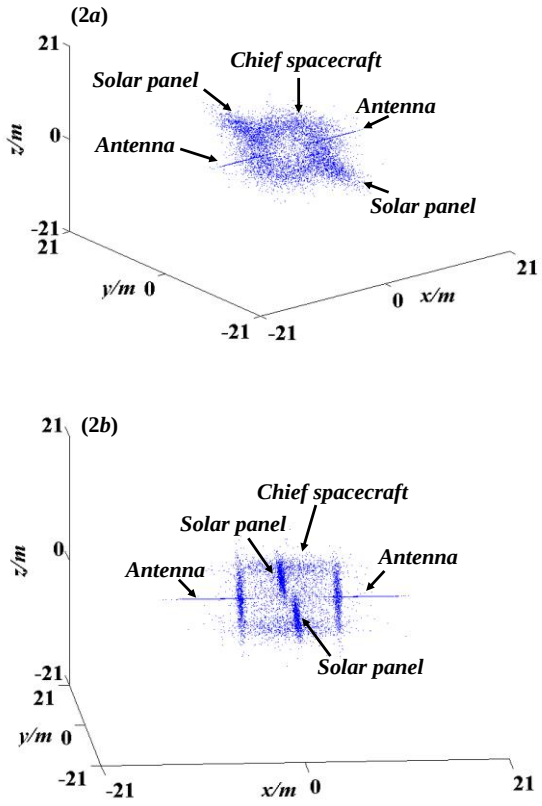

Fig.2 The 3D reconstruction of the chief with two solar panels and two antennas

Subsequently, based on the Eq.(8) with the parameters shown in **Appendix A4**, the GMM-based potential function in Eq. (8) is shown in Fig.3. The area marked with a green dotted line in Fig.3a is magnified and shown in Fig.3b. Moreover, the colorbars on Fig.3a and Fig.3b represent the changing values of GMM-based potential function in Eq.(8). As the antenna has important effects in this scenario, the number of the adopted feature point on the antenna for 3D construction is higher than the other parts of the chief spacecraft. Furthermore, the weights of the Gaussian model corresponding to antennas are larger than other parts, which is explicit in Eq.(36)-(38) where the values of the 7^{th} and 8^{th} weights π are larger than others. Thus, the values of GMM-based potential function in antenna much exceeds other parts' values. In addition, Fig.3 further verifies that the GMM-based potential function can consider the influence of the antenna.

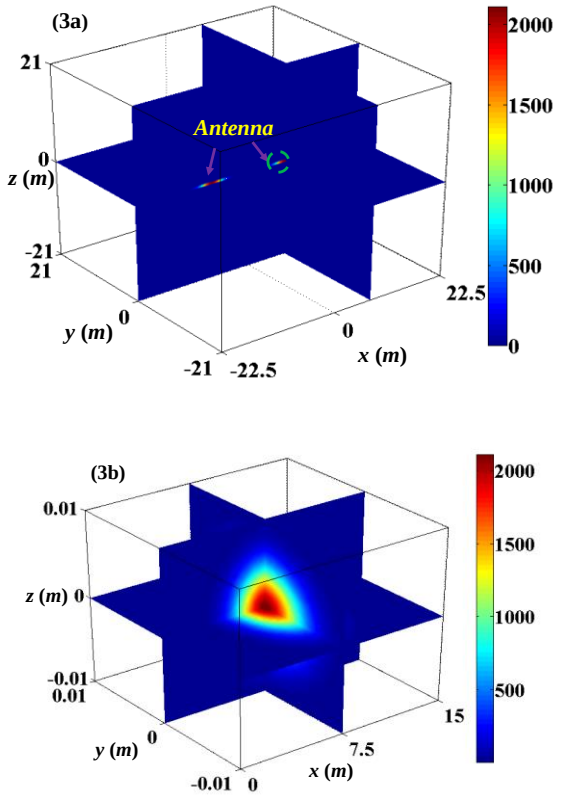

Fig.3 The GMM-based potential field: the area marked with a green dotted line in Fig.3a is magnified and shown in Fig.3b.

The proposed GMM-NTSMC approach is applied for spacecraft close-range proximity with obstacle avoidance in presence of a complex shape. In addition, the APF-TSMC and the GMM-TSMC are utilized for comparison. Fig. 4 shows the actual trajectory of the deputy spacecraft with APF-TSMC, GMM-TSMC and GMM-NTSMC. Moreover, Fig.4b and Fig.4c are magnifications of the region around the solar panel and the antenna, respectively. From Fig.4a and Fig.4b, the APF-TSMC, the GMM-TSMC and the GMM-NTSMC successfully avoid collision in presence of the solar panel. Based on Fig.4a and Fig.4c, the GMM-based avoidance maneuvers, which includes the GMM-TSMC and GMM-NTSMC, successfully avoid collision in the presence of the antenna while the APF-TSMC fails. It is because that the GMM-based potential function includes the available parameters of the complex shape obtained by the GMM method. Although the performance improvement of GMM-NTSMC cannot been fully shown

in the Fig. 4, it will be analyzed in Fig.5 with respect to the velocity change.

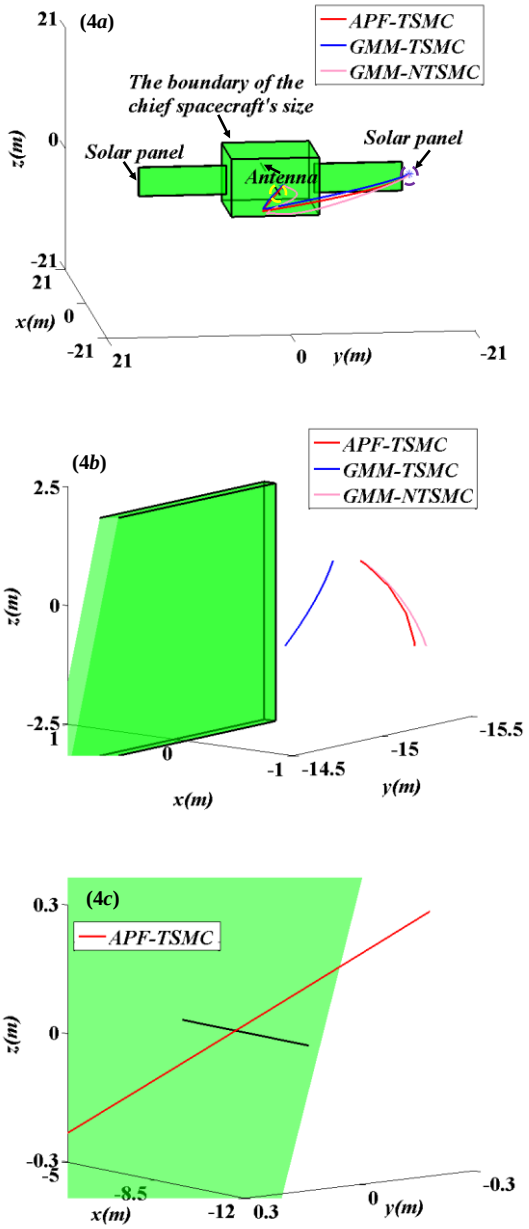

Fig.4 The actual trajectory of the deputy spacecraft: the areas marked with the purple dotted line and yellow dotted line in Fig.4a are magnified, Fig.4b and Fig.4c are magnifications of the region around the solar panel and the antenna, respectively.

Next, in order to assess the efficiency of the proposed control laws, the fuel cost can be utilized. It is generally known that the lifecycle of the spacecraft depends on the residual fuel. Thus, the control law

based on the less fuel cost will show the advantage of the proposed GMM-NTSMC. In this paper, the following mathematical model to compute the total velocity change and evaluate the control laws is given as

$$\delta v_{totoal} = \int_0^{t_f} \left(\delta \mathbf{v}^{\mathrm{T}} \delta \mathbf{v} \right)^{\frac{1}{2}} dt \tag{24}$$

Fig.5 shows the comparison of the total velocity change over 800s for the APF-TSMC, GMM-TSMC and GMM-NTSMC avoidance strategies. Though the APF-TSMC cannot solve the space-craft close-range proximity problem in presence of the antenna, it still has the highest total velocity change. Compared with APF-TSMC, the GMM based control not only guarantees the safety perfor-mance of this space mission, but also has lower total velocity change. This is because that the GMM-based potential function considers the influence of the chief spacecraft's complex shape, and hence the control forces generated by GMM-TSMC and GMM-NTSMC can avoid collision with the antenna and require less total velocity change. Furthermore, the GMM-TSMC and the GMM-NTSMC can further reduce to 56% and 54.47% the total velocity change with respect to the APF-TSMC, respec-tively. Though the GMM-TSMC and the GMM-NTSMC have the same control algorithm structure, the difference is that the switching surface of GMM-NTSMC is developed from the NTSMC [26]. However, the GMM-NTSMC requires a little more velocity change than the GMM-TSMC. The reason for this is that the GMM-NTSMC avoids the antenna and the solar panel at a greater distance compared with GMM-TSMC (as shown in Fig.4). In addition, as aforementioned analysis in Section III, the GMM-NTSMC can avoid a singularity problem while the GMM-TSMC cannot. Thus, the GMM-NTSMC would be a good choice to design an avoidance maneuver.

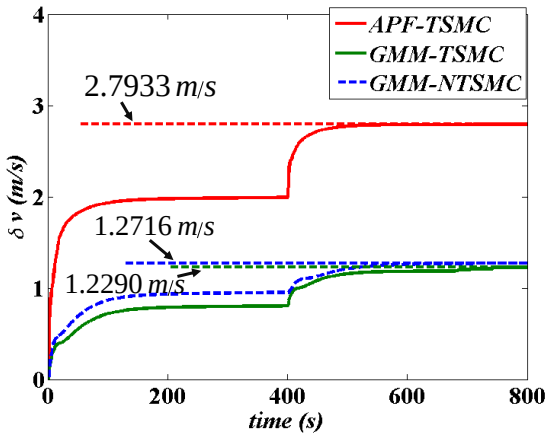

Fig.5 Total velocity change comparison between APF-TSMC, GMM-TSMC and GMM-NTSMC.

5 Conclusions

A Gaussian Mixture Model (GMM) based nonsingular terminal sliding mode control (NTSMC) (GMM-NTSMC) was proposed for safe spacecraft close-range proximity considering complex shape. Based on GMM, GMM-based potential function is designed for a complex geometry chief spacecraft. Compared with the artificial potential function (APF), the available parameters of the complex shape obtained by the GMM are included in the GMM-based potential function. Thus, the GMM based avoidance strategies, which are Gaussian Mixture Model based terminal sliding mode control (GMM-TSMC) and GMM-NTSMC, can solve the collision avoidance problem considering complex shape while APF-based control fails. Moreover, the GMM-based control requires the less total velocity change with respect to the APF-based control. Though the GMM-NTSMC requires more total velocity change than the GMM-TSMC, the proposed control retains the advantage of the NTSMC and can avoid singularity problem while GMM-TSMC cannot. To extend the application of the developed GMM-NTSMC, the determination of the number of Gaussian probability distribution functions and the designing control parameters should be researched.

Acknowledgements: The work was supported by the Major Program of National Nature Science Foundation of China under Grant Numbers 61690210 and 61690213, the National Science Foundation of China (Grant no. 11725211, 12002383 and 51675525), and the China Postdoctoral Science Foundation (Grant no. 2019M664019).

Reference

1 X. Y. Ji, Y. Z. Li, G. Q. Liu, et al. A brief review of ground and flight failures of Chinese spacecraft. Progress in Aerospace Science, 2019, 107: 19-29.

2 A. Ellery, J. Kreisel, B. Sommer. The case for robotic on-orbit servicing of spacecraft: spacecraft reliability is a myth. Acta Astronautica, 2008, 63(5): 632-648.

3 R. E. Rumford. Demonstration of autonomous rendezvous technology (DART) project summary. Proceedings of SPIE-The International Society for Optical Engineering, 2003, 5088: 10-19.

4 A. Flores-Abad, O. Ma, K. Pham, et al. A review of space robotics technologies for on-orbit servicing. Progress in Aerospace Sciences, 2014, 68(1)： 1-26.

5 W. J. Li, D. Y. Cheng, X. G. Liu, et al. On-orbit service (OOS) of spacecraft: a review of engineering developments. Progress in Aerospace Sciences, 2019, 108: 32-120.

6 J. R. Zhang, X. Y. Chu, Y. Zhang, et al. Safe-trajectory optimization and tracking control in ultra-close proximity to a failed satellite. Acta Astronautica, 2018, 144: 339-353.

7 B. Hua, Y. Huang, Y. H. Wu, et al. Spacecraft formation reconfiguration trajectory planning with avoidance constraints using adaptive pigeon-inspired optimization. Science China Information Sciences, 2019, 62: 070209:01-070209:3.

8 G. R. Frey, C. D. Petersen, F. A. Leve, et al. Constrained spacecraft relative motion planning exploiting periodic natural motion trajectories ad invariance. Journal of Guidance, Control, and Dynamics, 2017, 40(12): 3100-3115.

9 Y. Z. Luo and Z. J. Sun. Safe Rendezvous Scenario Design for Geostationary Satellites with Collision Constraints. Astrodynamics, 2017, 1(1): 71-83.

10 Y. Z. Luo, Z. J. Sun, J. Zhang. Proximity scenario design for geostationary rendezvous with collocated satellite avoidance. Acta Astronautica, 2019, 154: 153-168.

11 Q. Ni, Y. Y. Huang, X. Q. Chen. Nonlinear control of spacecraft formation flying with disturbance rejection and collision avoidance. Chinese Physics B, 2017, 26(1): 014502.

12 L. Cao, D. Qiao, J. W. Xu. Suboptimal artificial potential function sliding mode control for spacecraft rendezvous with obstacle avoidance. Acta Astronautica, 2018, 143: 133-146.

13 Y. Wang, Y. Z. Bai, J. J. Xing, et al. Equal-collision-probability-curve method for safe spacecraft close-range proximity maneuvers. Advance in Space Research, 2018, 62(9): 2599-2619.

14 Y. Wang, X. Q. Chen, Y. Z. Bai, et al. Motion planning of spacecraft with obstacle avoidance under low uncertainty using the improved equal-collision-probability-curve and improved linear quadratic regulator strategy. Proceedings of the Institution of Mechanical Engineers, Part G: Journal of Aerospace Engineering, 2019, 233(14): 5456-5467.

15 Y. Wang, X. Q. Chen, D. C. Ran, et al. Spacecraft formation reconfiguration with multi-obstacle avoidance under navigation and control uncertainties using adaptive artificial potential function method. Astrophysics, 2020, 4(1): 41-56.

16 G. X. Wen, C. L. Chen, H. Dou, et al. Formation control with obstacle avoidance of second-order multi-agent systems under directed communication topology. Science China Information Sciences, 2019, 62(9): 192205:1-192205: 14.

17 X. Z. Bai, C. W. Ma, L. Chen, et al. Maximum collision probability considering variable size, shape, and orientation of covariance ellipse. Advance in Space Research, 2016, 58(6): 950-966.

18 Y. Wang, X. Q. Chen, D. C. Ran, et al. Multi-equal-collision-probability-curve method for convex polygon shape spacecraft safe proximity maneuvers. Journal of Navigation, 2019, 72(2): 405-429.

19 Y. Wang, Y. Z. Bai, D. C. Ran, et al. Dual-equal-collision-probability-curve method for spacecraft safe proximity maneuvers in presence of complex shape. Acta Astronautica, 2019, 159: 65-76.

20 D. Lau, E. Jonathan, O. Denny. Fluid motion planner for nonholonomic 3-D mobile robots with kinematic constraints. IEEE Transactions on Robotics, 2015, 31(6): 1537-1547.

21 B. Eckart. Compact generative models of point cloud data for 3D perception. Ph.D dissertation, The Robotics Institute, Carnegie Mellon University, Pittsburgh, Pennsylvania, 2016.

22 X. Z. Zhu. Research on vision based close-range sensing of uncooperative targets. Ph.D dissertation, College of Aeronautics and Astronautics, National University of Defense Technology, Changsha, Hunan Province, China, 2017. (in Chinese)

23 V. Vittaldev, R. P. Russell, R. Linares. Spacecraft uncertainty propagation using Gaussian Mixture Models and polynomial Chaos Expansions. Journal of Guidance, Control, and Dynamics, 2016, 39(12): 2615-2626.

24 Y. Z. Luo, Z. Yang. A review of uncertainty propagation in orbital mechanics. Progress in Aerospace Sciences, 2017, 89: 23-39.

25 J. Yu. A nonlinear kernel Gaussian Mixture Model based inferential monitoring approach for fault detection and diagnosis of chemical processes. Chemical Engineering Science, 2012, 16(1): 506-519.

26 M. Van, S. S. Sam, H. L. Ren. Finite time fault tolerant control for robot manipulators using time delay estimation and continuous nonsingular fast terminal sliding mode control. IEEE Transaction on Cybernetics, 2017, 47(7): 1681-1693.

27 B. Y. Li. An experiment of *K*-means initialization strategies on handwritten digits dataset. Intelligent Information Management, 2018, 10(2): 43-44.

28 A. P. Dempster, N. M. Laird, D. B. Rubin. Maximum likelihood from incomplete data via the EM Algorithm. *J*ournal of the Royal Statistical Society, 1977, 39(1): 1-38.

29 L. C. Feng, Y. Z. Bai, X. Q. Chen. Finite-time sliding mode control for spacecraft rendezvous with collision avoidance. Journal of Astronautics, 2016, 37(11): 1342-1348. (in Chinese)

30 L. Cao, X. Q. Chen, A. K. Misra. Minimum sliding mode error feedback control for fault tolerant reconfigurable satellite formations with J2 perturbations. Acta Astronautica, 2014, 96: 201-216.

31 L. Cao L, X. Q. Chen, Z. D. Zhang, et al. Predictive smooth variable structure filter for attitude synchronization estimation during satellite formation flying. IEEE Transactions on Aerospace and Electronic, 2017, 53(3): 1375-1383.

32 K. Yamanaka and F. Ankersen. New state transition matrix for relative motion on an arbitrary elliptical orbit. Journal of Guidance, Control, and Dynamics, 2002, 25(1): 60-66.

33 Y. M. Fu, W. Li, G. R. Duan. Satellite trajectory model reference output tracking control based on T-H equation. Journal of Astronautics, 2013, 34(4): 496-502. (in Chinese)

Appendix A1

Based on the definition of the final GMM-based potential function φ, the gradient $\nabla_r\varphi$ can be deduced from Eq.(9) with respect to the relative position vector $\boldsymbol{r}$ of the deputy spacecraft, which is given as

$$\begin{aligned}\nabla_r\varphi=&\boldsymbol{P}\left(\boldsymbol{r}-\boldsymbol{r}_f\right)+\boldsymbol{M}\left(\boldsymbol{r}-\boldsymbol{r}_f\right)\sum_{j=1}^{K}\frac{\pi_j}{2\pi\left|\boldsymbol{\Sigma}_j\right|^{1/2}}e^{-\frac{1}{2}\left(\boldsymbol{r}-\boldsymbol{\mu}_j\right)^{\mathrm{T}}\boldsymbol{\Sigma}_j^{-1}\left(\boldsymbol{r}-\boldsymbol{\mu}_j\right)}\\&-\frac{1}{2}\left(\boldsymbol{r}-\boldsymbol{r}_f\right)^{\mathrm{T}}\boldsymbol{M}\left(\boldsymbol{r}-\boldsymbol{r}_f\right)\sum_{j=1}^{K}\frac{\pi_j}{2\pi\left|\boldsymbol{\Sigma}_j\right|^{1/2}}e^{-\frac{1}{2}\left(\boldsymbol{r}-\boldsymbol{\mu}_j\right)^{\mathrm{T}}\boldsymbol{\Sigma}_j^{-1}\left(\boldsymbol{r}-\boldsymbol{\mu}_j\right)}\boldsymbol{\Sigma}_j^{-1}\left(\boldsymbol{r}-\boldsymbol{\mu}_j\right).\end{aligned}\tag{25}$$

To obtain the derivation of the switching surface, any components of $\boldsymbol{S}$ should be derived in Eq.(11). The detailed mathematical expressions of the symbol $\nabla_{rr}\varphi$ and $\nabla_{rr_f}\varphi$ are given as

$$\begin{aligned}\nabla_{\boldsymbol{rr}}\varphi=&\boldsymbol{P}+\boldsymbol{M}\sum_{j=1}^{K}\frac{\pi_j}{2\pi\left|\boldsymbol{\Sigma}_j\right|^{1/2}}e^{-\frac{1}{2}\left(\boldsymbol{r}-\boldsymbol{\mu}_j\right)^{\mathrm{T}}\boldsymbol{\Sigma}_j^{-1}\left(\boldsymbol{r}-\boldsymbol{\mu}_j\right)}-\left(\sum_{j=1}^{K}\frac{\pi_j}{2\pi\left|\boldsymbol{\Sigma}_j\right|^{1/2}}e^{-\frac{1}{2}\left(\boldsymbol{r}-\boldsymbol{\mu}_j\right)^{\mathrm{T}}\boldsymbol{\Sigma}_j^{-1}\left(\boldsymbol{r}-\boldsymbol{\mu}_j\right)}\boldsymbol{\Sigma}_j^{-1}\left(\boldsymbol{r}-\boldsymbol{\mu}_j\right)\right)\left(\boldsymbol{r}-\boldsymbol{r}_f\right)^{\mathrm{T}}\boldsymbol{M}\\&-\boldsymbol{M}\left(\boldsymbol{r}-\boldsymbol{r}_f\right)\left(\sum_{j=1}^{K}\frac{\pi_j}{2\pi\left|\boldsymbol{\Sigma}_j\right|^{1/2}}e^{-\frac{1}{2}\left(\boldsymbol{r}-\boldsymbol{\mu}_j\right)^{\mathrm{T}}\boldsymbol{\Sigma}_j^{-1}\left(\boldsymbol{r}-\boldsymbol{\mu}_j\right)}\left(\boldsymbol{r}-\boldsymbol{\mu}_j\right)^{\mathrm{T}}\boldsymbol{\Sigma}_j^{-\mathrm{T}}\right)\\&+\frac{1}{2}\left(\boldsymbol{r}-\boldsymbol{r}_f\right)^{\mathrm{T}}\boldsymbol{M}\left(\boldsymbol{r}-\boldsymbol{r}_f\right)\sum_{j=1}^{K}\frac{\pi_j}{2\pi\left|\boldsymbol{\Sigma}_j\right|^{1/2}}e^{-\frac{1}{2}\left(\boldsymbol{r}-\boldsymbol{\mu}_j\right)^{\mathrm{T}}\boldsymbol{\Sigma}_j^{-1}\left(\boldsymbol{r}-\boldsymbol{\mu}_j\right)}\left[\boldsymbol{\Sigma}_j^{-1}\left(\boldsymbol{r}-\boldsymbol{\mu}_j\right)\left(\boldsymbol{r}-\boldsymbol{\mu}_j\right)^{\mathrm{T}}\boldsymbol{\Sigma}_j^{-\mathrm{T}}-\boldsymbol{\Sigma}_j^{-1}\right].\end{aligned}\tag{26}$$

$$\begin{aligned}\nabla_{\boldsymbol{rr}_f}\varphi=&-\boldsymbol{P}-\boldsymbol{M}\sum_{j=1}^{K}\frac{\pi_j}{2\pi\left|\boldsymbol{\Sigma}_j\right|^{1/2}}e^{-\frac{1}{2}\left(\boldsymbol{r}-\boldsymbol{\mu}_j\right)^{\mathrm{T}}\boldsymbol{\Sigma}_j^{-1}\left(\boldsymbol{r}-\boldsymbol{\mu}_j\right)}\\&-\boldsymbol{M}\left(\boldsymbol{r}-\boldsymbol{r}_f\right)\sum_{j=1}^{K}\frac{\pi_j}{2\pi\left|\boldsymbol{\Sigma}_j\right|^{1/2}}e^{-\frac{1}{2}\left(\boldsymbol{r}-\boldsymbol{\mu}_j\right)^{\mathrm{T}}\boldsymbol{\Sigma}_j^{-1}\left(\boldsymbol{r}-\boldsymbol{\mu}_j\right)}\left(\boldsymbol{r}-\boldsymbol{\mu}_j\right)^{\mathrm{T}}\boldsymbol{\Sigma}_j^{-\mathrm{T}}.\end{aligned}\tag{27}$$

Appendix A2

The APF is a defined scalar function and is consist of attractive potential and repulsive potential. According to the Lyapunov stability theorem, the derivation of APF can guarantee the system speed and position converge to the desired and does not violate the obstacle constraint. Based on the Ref. [12, 29], the APF is given as

$$\varphi_1=\frac{1}{2}\left(\boldsymbol{r}-\boldsymbol{r}_f\right)^{\mathrm{T}}\boldsymbol{P}\left(\boldsymbol{r}-\boldsymbol{r}_f\right)+\frac{1}{2}\left(\boldsymbol{r}-\boldsymbol{r}_f\right)^{\mathrm{T}}\boldsymbol{M}\left(\boldsymbol{r}-\boldsymbol{r}_f\right)\sum_{i=1}^{m}\psi_i\exp\left[-\frac{\left(\boldsymbol{r}-\boldsymbol{r}_{obs,i}\right)^{\mathrm{T}}\boldsymbol{N}_i\left(\boldsymbol{r}-\boldsymbol{r}_{obs,i}\right)}{\sigma_i}\right],\tag{28}$$

where m is the number of the obstacle. $\boldsymbol{r}_{obs,i}$ is the position center of the obstacle i^{th} . The parameters ψ_i and σ_i determine the overall height and width of the repulsive potential. The matrix $\boldsymbol{N}_i$ is a positive definite matrix and determines the oblateness and orientation of the Gaussian function. The magnitude of the matrix $\boldsymbol{N}_i$ determines how sharply the repulsive potential decays with distance from the obstacle center.

Based on Eq.(28), the switching surface of the APF-TSMC [12, 29], is given as

$$\boldsymbol{S}_1=\boldsymbol{k}_s\nabla_{\boldsymbol{r}}\varphi_1+\dot{\boldsymbol{e}},\tag{29}$$

where $\nabla_r \varphi_1$ is the gradient of APF φ_1 with respect to the position vector of the deputy spacecraft and the detailed mathematical expressions is shown in Ref. [29].

Moreover, the asymptotic law of the APF-TSMC is chosen as Eq.(12). Thus, the control law of the APF-TSMC is obtained as

$$\boldsymbol{u}_1 = -\boldsymbol{k}_s \left(\nabla_{rr} \varphi_1 \dot{\boldsymbol{r}} + \nabla_{rr_f} \varphi_1 \dot{\boldsymbol{r}}_f \right) - \boldsymbol{A}\boldsymbol{r} - \boldsymbol{B}\dot{\boldsymbol{r}} - \boldsymbol{\lambda}_1 \boldsymbol{S}_1 - \boldsymbol{\lambda}_2 sig\left(\boldsymbol{S}_1\right)^{\alpha} + \ddot{\boldsymbol{r}}_f , \tag{30}$$

where the mathematical expressions of $\nabla_{rr} \varphi$ and $\nabla_{rr_f} \varphi$ are derived in Ref. [29].

In addition, based on Ref. [12], the finite convergence time is obtained.

Appendix A3

According to the gradient of GMM-based potential function and the TSMC, the switching surface of GMM-TSMC is designed as

$$\boldsymbol{S}_2 = \boldsymbol{k}_s \nabla_r \varphi + \dot{\boldsymbol{e}}. \tag{31}$$

Subsequently, the asymptotic law of the GMM-TSMC is chosen as Eq.(12). Thus, the control law of the GMM-TSMC is obtained as

$$\boldsymbol{u}_2 = -\boldsymbol{k}_s \left(\nabla_{rr} \varphi \dot{\boldsymbol{r}} + \nabla_{rr_f} \varphi \dot{\boldsymbol{r}}_f \right) - \boldsymbol{A}\boldsymbol{r} - \boldsymbol{B}\dot{\boldsymbol{r}} - \boldsymbol{\lambda}_1 \boldsymbol{S}_2 - \boldsymbol{\lambda}_2 sig\left(\boldsymbol{S}_2\right)^{\alpha} + \ddot{\boldsymbol{r}}_f . \tag{32}$$

To analyze the stability of the GMM-TSMC, a Lyapunov function is defined as

$$V_2 = \frac{1}{2} \boldsymbol{S}_2^{\mathrm{T}} \boldsymbol{S}_2 \geq \boldsymbol{0}. \tag{33}$$

Based on Eq.(33),

$$\dot{V}_2 = \boldsymbol{S}_2^{\mathrm{T}} \dot{\boldsymbol{S}}_2 = -\boldsymbol{S}_2^{\mathrm{T}} \left(\boldsymbol{\lambda}_1 \boldsymbol{S}_2 + \boldsymbol{\lambda}_2 sig\left(\boldsymbol{S}_2\right)^{\alpha} \right) \leq -\lambda_{1\min} \boldsymbol{S}_2^{\mathrm{T}} \boldsymbol{S}_2 - \lambda_{2\min} \left\| \boldsymbol{S}_2 \right\|^{\alpha+1}. \tag{34}$$

According to **Lemma 1**,

$$\begin{aligned}\dot{V}_2 &\le -\lambda_{1\min}\boldsymbol{S}_2^{\mathrm{T}}\boldsymbol{S}_2 - \lambda_{2\min}\left\|\boldsymbol{S}_2\right\|^{\alpha+1} \le -2\lambda_{1\min}V_2 - \lambda_{2\min}\left(2V_2\right)^{\frac{\alpha+1}{2}} \\ &\le -2\lambda_{1\min}V_2 - \sqrt{2}\lambda_{2\min}V_2^{\frac{1}{2}}.\end{aligned} \tag{35}$$

Therefore, by the Lyapunov stability theorem, the system with GMM-TSMC is stable in finite time [12].

Appendix A4

The parameters of the GMM shown in Eq.(8) are given as

$$\pi = \left[\pi_{11} \quad \pi_{12}\right], \tag{36}$$

$$\pi_{11} = \left[7.7216\times10^{-2} \quad 7.7216\times10^{-2} \quad 7.7456\times10^{-2} \quad 7.7456\times10^{-2} \quad 7.7217\times10^{-2}\right], \tag{37}$$

$$\pi_{12} = \left[7.7217\times10^{-2} \quad 1.9113\times10^{-1} \quad 1.9113\times10^{-1} \quad 7.6980\times10^{-2} \quad 7.6980\times10^{-2}\right], \tag{38}$$

$$\boldsymbol{u} = \left[\boldsymbol{u}_{11} \quad \boldsymbol{u}_{12}\right], \tag{39}$$

$$\boldsymbol{u}_{11} = \begin{bmatrix} 5 & -5 & 0 & 0 & 0 \\ 0 & 0 & 5 & -5 & 0 \\ 0 & 0 & 0 & 0 & 5 \end{bmatrix}, \tag{40}$$

$$\boldsymbol{u}_{12} = \begin{bmatrix} 0 & -7.5 & 7.5 & 0 & 0 \\ 0 & 0 & 0 & 10.02 & -10.02 \\ -5 & 0 & 0 & 0 & 0 \end{bmatrix}, \tag{41}$$

$$\boldsymbol{\Sigma}(:,:,1)=\begin{bmatrix}1\times10^{-5} & 0 & 0\\ 0 & 8.4169 & 0\\ 0 & 0 & 8.4169\end{bmatrix},\boldsymbol{\Sigma}(:,:,2)=\begin{bmatrix}1\times10^{-5} & 0 & 0\\ 0 & 8.4169 & 0\\ 0 & 0 & 8.4169\end{bmatrix},$$

$$\boldsymbol{\Sigma}(:,:,3)=\begin{bmatrix}8.3907 & 0 & 0\\ 0 & 1\times10^{-5} & 0\\ 0 & 0 & 8.3971\end{bmatrix},\ \boldsymbol{\Sigma}(:,:,4)=\begin{bmatrix}8.3907 & 0 & 0\\ 0 & 1\times10^{-5} & 0\\ 0 & 0 & 8.3971\end{bmatrix},$$

$$\boldsymbol{\Sigma}(:,:,5)=\begin{bmatrix}8.4167 & 0 & 0\\ 0 & 8.4166 & 0\\ 0 & 0 & 1\times10^{-5}\end{bmatrix},\ \boldsymbol{\Sigma}(:,:,6)=\begin{bmatrix}8.4167 & 0 & 0\\ 0 & 8.4166 & 0\\ 0 & 0 & 1\times10^{-5}\end{bmatrix},$$

$$\boldsymbol{\Sigma}(:,:,7)=\begin{bmatrix}2.0834 & 0 & 0\\ 0 & 1\times10^{-5} & 0\\ 0 & 0 & 1\times10^{-5}\end{bmatrix},\ \boldsymbol{\Sigma}(:,:,8)=\begin{bmatrix}2.0834 & 0 & 0\\ 0 & 1\times10^{-5} & 0\\ 0 & 0 & 1\times10^{-5}\end{bmatrix},$$

$$\boldsymbol{\Sigma}(:,:,9)=\begin{bmatrix}1\times10^{-5} & 0 & 0\\ 0 & 8.3653 & 0\\ 0 & 0 & 2.1044\end{bmatrix},\ \boldsymbol{\Sigma}(:,:,10)=\begin{bmatrix}1\times10^{-5} & 0 & 0\\ 0 & 8.3653 & 0\\ 0 & 0 & 2.1044\end{bmatrix}. \tag{42}$$